#### **NURETH14-290**

### MELT ERUPTION MODELING FOR MCCI SIMULATIONS

### K. Robb, M. Corradini

University of Wisconsin-Madison, WI, U.S.A.

#### **Abstract**

This paper presents results of an investigation into the melt eruption phenomenon that could occur during molten corium concrete interactions (MCCI). Melt eruptions have occurred during many laboratory scale MCCI tests and have a large potential impact on the accident progression. The results of a low temperature experimental investigation of melt eruptions are provided. Models which predict melt entrainment and the number of eruption sites are presented.

#### Introduction

The probability and timing of containment failure during a nuclear power plant severe accident has a large impact on the potential of radiological releases. If an accident progresses to the point of an ex-vessel core melt, the concrete basemat of containment can be thermally attacked by the molten core materials (corium). The rate of concrete ablation and the release of steam and non-condensables impact the probability and timing of containment failure. Several international research programs have investigated molten corium concrete interactions (MCCI) in order to understand and reduce the uncertainties of such an accident scenario. Through these research programs phenomena such as water ingression, bulk crust failure, and melt eruptions have been observed to augment the coolability of the core debris [1].

During the early stages of MCCI, the surface of the melt is vigorously agitated by gases from the decomposition of the underlying concrete. As time progresses, the melt cools and a porous crust forms and floats on the surface of the melt. As the decomposition gases pass through holes or cracks in the crust, melt can be ejected from the melt pool onto the crust surface. This process is illustrated in Figure 1 and is known as the melt eruption, ejection, or entrainment phenomenon. eruptions are a beneficial mechanism as it transports hot melt from below the insulating crust and transforms it into a more coolable geometry. The impact and occurrence of melt eruptions during experiments have been previously reviewed [2, 1, 12].

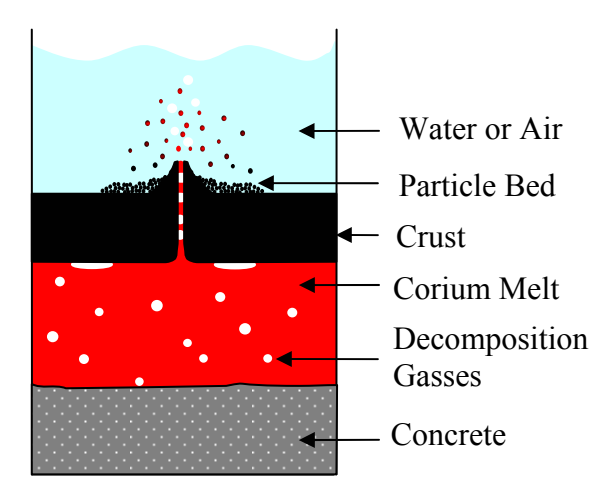


**Figure 1: Melt Eruption Illustration** 

Melt eruption modeling has advanced from empirical to phenomenological based models [2, 3, 4, 5]. Melt eruption modeling has been divided into two parts, entrainment and flow geometry. Entrainment involves determining the amount of melt ejected given a predicted flow geometry and gas flow rate. The flow geometry refers to determining the number and size of eruption sites. This paper presents a system of equations (provided other MCCI system information) to predict the number of eruption sites and the entrainment of melt through them. A model to determine the eruption site diameter was investigated; however, the uncertainty in the boundary conditions dominated the predictions.

### 1. Entrainment

A method to quantify the rate of melt ejection is through defining the melt entrainment coefficient, Ke, Eqn. (1). Through knowledge of the entrainment coefficient and the volumetric gas flow rate, the ejected melt flow rate can be determined. It has been proposed the bulk crust is permeable to gas [5]. The superficial gas velocity through the eruption sites can be determined through knowledge of the gas velocity in the pool (concrete composition and decomposition rate) the number and diameter of channels (see Section 2) and the gas velocity through the bulk crust (see [5]), Eqn. (2). This relation assumes there all of the eruption sites are the same size and the gas flow is evenly distributed to the channels. Using Eqns. (1, 2), the entrainment coefficient of the channel and pool can be related, Eqn. (3). If a negligible fraction of gases pass through the porosity in the crust, the pool and channel entrainment coefficients are equal. The submergence, defined by Eqn. (4), is a convenient non-dimensional form of the driving pressure across the channel.

$$Ke = \frac{\dot{V}_{m}}{\dot{V}_{g}} = \frac{\dot{J}_{m} \cdot A}{\dot{J}_{g} \cdot A} = \frac{\dot{J}_{m}}{\dot{J}_{g}}$$
 (1)

$$j_{g,ch} = \frac{A_{cr}}{A_{ch total}} \cdot \left(j_{g,pool} - j_{g,cr}\right) = \frac{4 \cdot A_{cr}}{N_{ch} \cdot \pi \cdot d_{ch}^2} \cdot \left(j_{g,pool} - j_{g,cr}\right)$$
(2)

$$Ke_{pool} = Ke_{ch} \left( 1 - \frac{\dot{V}_{g,cr}}{\dot{V}_{g,pool}} \right) \approx Ke_{ch} \left( 1 - \frac{\dot{J}_{g,cr}}{\dot{J}_{g,pool}} \right)$$
(3)

$$S = \frac{\Delta P_{ch}}{\rho_{m} \cdot g \cdot \delta_{ch}} = \frac{\rho_{cr} \cdot \delta_{cr} + \rho_{pb} \cdot \delta_{pb}}{\rho_{m} \cdot \delta_{ch}}$$
(4)

### 1.1 Facility Description

The UW entrainment facility was designed taking into account the experience gained and challenges encountered by the PERCOLA research program [3, 4]. The purpose of the facility was to expand the experimental database from the PERCOLA program to aide in verifying a phenomenological entrainment model.

Similar to the PERCOLA facility, there is an inner tank (0.5m x 0.5m sq. inner dimensions) within a larger external tank (1.2m ID), Figure 2. Dry air is injected into the inner tank through

36x 0.6mm ID orifices. The gas flow rate is measured using three Aalborg thermal mass flow meters (GFM-37, 47, and 67). The gas rises 70 cm up to a Plexiglas plate, coalesces, and passes through an interchangeable acrylic flow channel. The entrained liquid is collected and continuously drained. To measure the liquid flow rate, timed samples are taken from the liquid stream and the mass of the sample is measured with a scale (OHAUS Scout Pro SP6001). With known liquid and gas flow rates, the time averaged entrainment coefficient, Eqn. (1), can be determined. The UW facility took the approach that a floating crust could be simulated by adjusting the under crust (plate) pressure of a rigid test stand. This setup minimized vibrations and allowed for steady boundary conditions. A differential pressure transducer (Rosemount 3051-CD) measures the driving pressure drop across the channel. The measured driving pressure is used in Eqn. (4) to determine the submergence. The liquid level in the tank could be raised or lowered to adjust the driving pressure across the channel. The uncertainty in the UW entrainment coefficient data was dominated by the uncertainty of the gas flow measurement. The minimum, maximum, and mean uncertainty of the entrainment coefficient data and gas flow rates were 1.0%, 32.4%, and 4.2%, respectively. The minimum, maximum, and mean uncertainty of the submergence was 0.2%, 14.8%, and 4.1%, respectively. Table 1 summarizes the range of parameters investigated by the PERCOLA program, the range investigated by the UW entrainment facility to date, and the approximate ranges which may be encountered during MCCI.

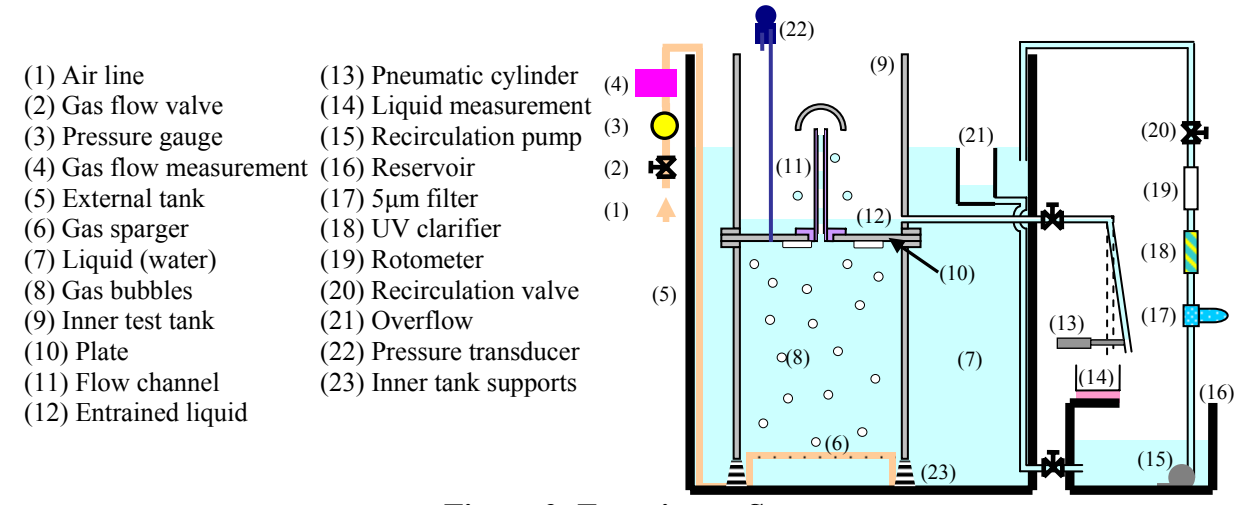


**Figure 2: Experiment Setup** 

### 1.2 Experiment Entrainment Results

The entrainment coefficient correlates well with the superficial channel velocity in contrast to the superficial pool velocity. This suggests the entrainment coefficient is dependent upon the two-phase behavior in the channel  $(j_{g,ch})$  and not the two-phase behavior in the pool  $(j_{g,pool})$ . This supports decoupling the eruption sites from the pool characteristics. The multi-channel and system scaling data support this finding, Figure 6-8.

Increasing submergence, Eqn. (4), (increasing the driving pressure across the channel) always increased entrainment, Figure 3. The entrainment coefficient generally decreases with increasing channel superficial gas velocity. The only exception observed was for large channels at low submergences (observed for S=30%,  $d_{ch}=2.54$ cm), for which the entrainment first increases and then decreases with increasing channel superficial gas velocity.

**Table 1: System Variables** 

Parameter	PERCOLA	UW	MCCI	Units
	[3, 4]		system	
Gas Flow Rate	11-2550	1-373		LPM
Pool superficial gas vel.	0.1-22	0.0068-7.8	0-10	cm/s
Ch. superficial gas vel.	0.1-22	0.060-44		m/s
Submergence	30-80	20-131	0-100+	%
Number of Channels	5.1, 15.3	4, 8, 12, 16	0-100+	$1/\mathrm{m}^2$
Channel Diameter	2.9, 5.0	0.93-2.57	0.1-1.0+	cm
Channel Length	5, 50	10-50	~5–100+	cm
Channel Entrance Geom.	90°	90°	Rounded?	-
Channel Material	Unspecified	Acrylic, Teflon, Glass	Semi-frozen melt	-
Sub-Plate Surface	Flat & Smooth	Flat & Smooth	Unknown?	-
Liquid Viscosity	0.001-0.300	0.001	0.001-solid	Pa s
Liquid Surface Tension	0.02-0.07	0.072	0.5-1.0	N/m
Liquid Density	960-1000	998.12	4000-6000	kg/m <sup>3</sup>

At a constant channel superficial gas velocity, varying the channel diameter had a second order impact on the entrainment, Figure 4. However, an exception was found for low submergences (<30%) where an increase in channel diameter led to a decrease in entrainment for channel superficial gas velocities below approximately 3 m/s. This decrease in entrainment may be due to changes in flow pattern within the channel.

Tests were performed with 1, 2, 3, and 4 channels 30 cm long, 1.58 cm ID, and at 60% submergence. As shown in Figures 7 and 8, the data correlates well with the channel superficial gas velocity and not the pool superficial gas velocity. In addition, the entrainment coefficient was nearly independent of the number of channels present. This finding aides in decoupling channels from one another.

During MCCI the length of the channel can increase simultaneously by buildup of frozen melt on the crust surface and through crust growth. By increasing the channel length, either the submergence and/or the total driving pressure must change. In one limit, the driving pressure across the channel would remain constant if the channel length is increased due to a buildup of melt forming a narrow cone-like mound (negligible increase in crust mass). For the other limit, the submergence would remain constant if there was uniform buildup of melt on the crust surface and the channel length increased solely due to crust growth (assuming crust and melt densities remain constant). If the channel length is increased while holding the submergence constant, entrainment increases, Figure 5. If the channel length increases while holding the driving pressure constant, the entrainment decreases.

Some tests were repeated using three different tube materials, acrylic, glass, and PTFE (Teflon). The channels all had nearly identical entrainment which suggests entrainment is independent of the melt-wall contact angle. The contact angle is function of temperature and liquid properties and is unknown for the MCCI melt eruption system.

To check scaling effects, tests were performed with a smaller test setup with an inner tank of 28.25 cm diameter and an external tank of 45.7 cm diameter. This inner tank is approximately one quarter the area of the larger facility. For the same conditions ( $j_{g,ch}$ ,  $\delta_{ch}$ ,  $d_{ch}$ , S) the

entrainment coefficients of the two facilities are very similar, Figure 6. The data does not correlate well with respect to the pool superficial gas velocity.

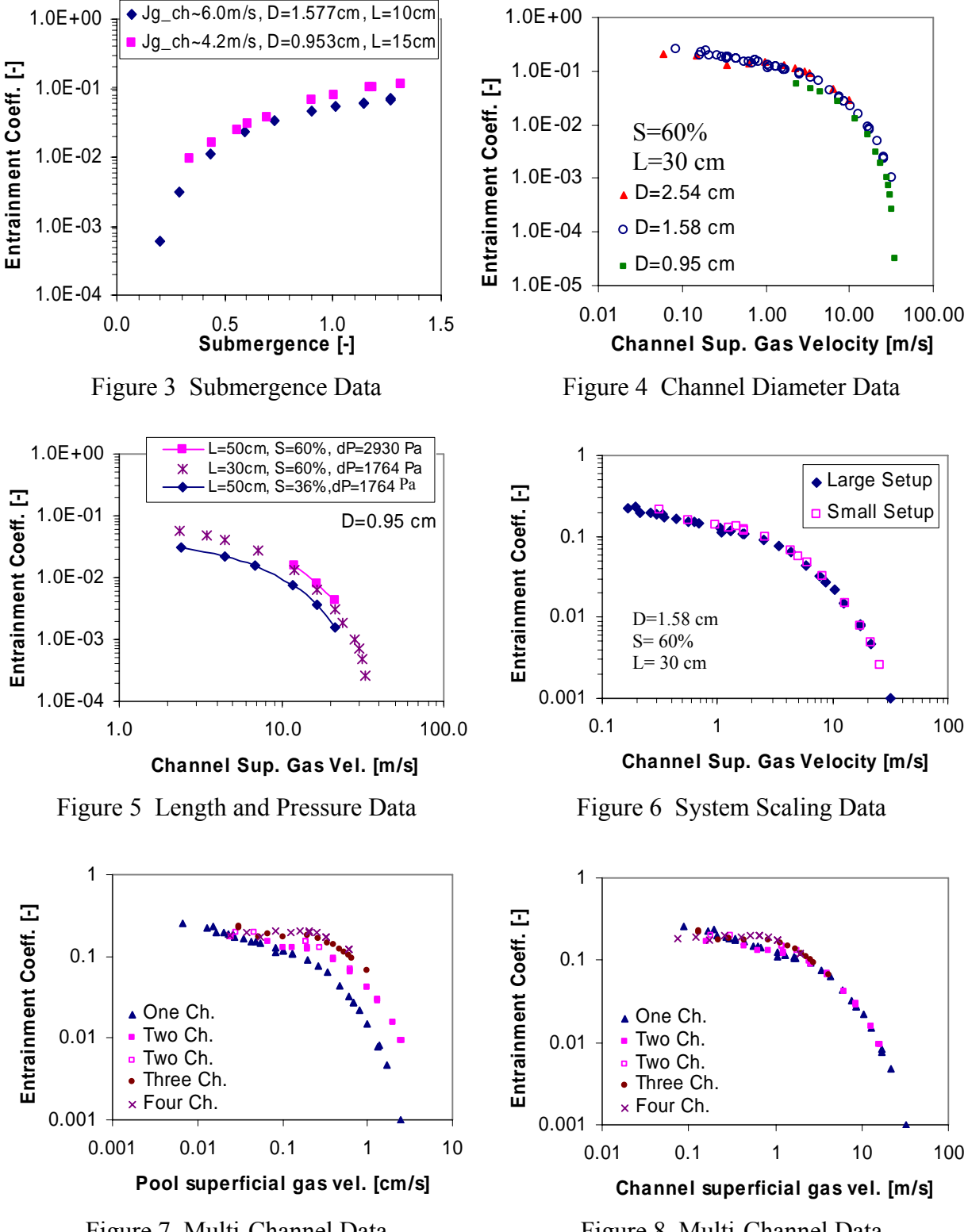


Figure 7 Multi-Channel Data Figure 8 Multi-Channel Data

## 1.3 Entrainment Modeling

To model the entrainment of liquid through the channel, a method similar to the PERCOLA Jet model [3, 4] has been pursued. The main differences are the form of the drift flux model and the inclusion of an acceleration pressure loss term. Assuming constant properties and geometry across the channel length, the pressure drop balance across any eruption site channel may be written as Eqn. (5).

$$\Delta P_{\text{driving}} = \Delta P_{\text{static}} + \Delta P_{\text{friction}} + \Delta P_{\text{singular}} + \Delta P_{\text{acceleration}}$$
 (5)

$$\Delta P_{\text{driving}} = \rho_{\text{m}} \cdot S \cdot \delta_{\text{ch}} \cdot g \tag{6}$$

Based on the submergence, the driving pressure drop across the channel is given by Eqn. (6). The static or gravitational pressure drop across the riser is given by Eqn. (7). The flow pattern within the channel during the air-water tests included slug, churn, and annular flow. At some conditions, the flow pattern was observed to vary from slug to churn to annular flow in less than a second. The drift-flux model by Dix, as described in [6], was chosen to determine the channel void fraction, Eqn. (8). The Dix model as described in [6] was used to determine distribution parameter and drift velocity Eqns. (9-10). This relatively simple model performed well when compared against air-water and steam experimental void fraction data, including high void fractions [6].

$$\Delta P_{\text{static}} = (\rho_{\sigma} \cdot \alpha + \rho_{m} \cdot (1 - \alpha)) \cdot g \cdot \delta_{ch} \approx \rho_{m} \cdot (1 - \alpha) \cdot g \cdot \delta_{ch}$$
 (7)

$$\alpha = \frac{j_{g,ch}}{j_{g,ch} \cdot \left(1 + \left(\frac{j_{m,ch}}{j_{g,ch}}\right)^{(\rho_g/\rho_m)^{0.1}}\right) + 2.9 \cdot \left(\frac{\sigma \cdot g}{\rho_1}\right)^{1/4}}$$
 (8)

The two-phase pressure drop, Eqn. (9), is determined by multiplying the single phase frictional pressure drop of the melt (second term in Eqn. (9)) by a two-phase multiplier (first term in Eqn. (9)). In this work, the value of 'n' is taken to equal 2.0 the same as in the PERCOLA model, [4]. The gas and melt entrance and exit losses have been treated separately and included as Eqn. (10). Using separate gas and liquid entrance and exit losses aides the model to account for all gas (gas buildup) and all liquid (sinking crust) flow conditions. The experimental data of this work was best reproduced by using a  $K_s$  value of 2.0. The acceleration pressure drop, due to the energy needed to accelerate the melt from rest to the channel velocity, has been accounted for through Eqn. (11). An equation for the superficial melt velocity in the channel, Eqn. (12), can be created by combining Equations (5-11). Eqn. (12) along with Eqn. (2) can be solved iteratively for  $j_{m,ch}$  for a given set of system conditions ( $j_{g,pool}$ ,  $\delta_{ch}$ ,  $N_{ch}$ ,  $d_{ch}$ , S). With  $j_{g,ch}$  and  $j_{m,ch}$  known, the entrainment coefficient can be determined using Eqn. (1). Note the liquid void fraction (1- $\alpha$ ) must be less than the submergence, S, for liquid to be entrained.

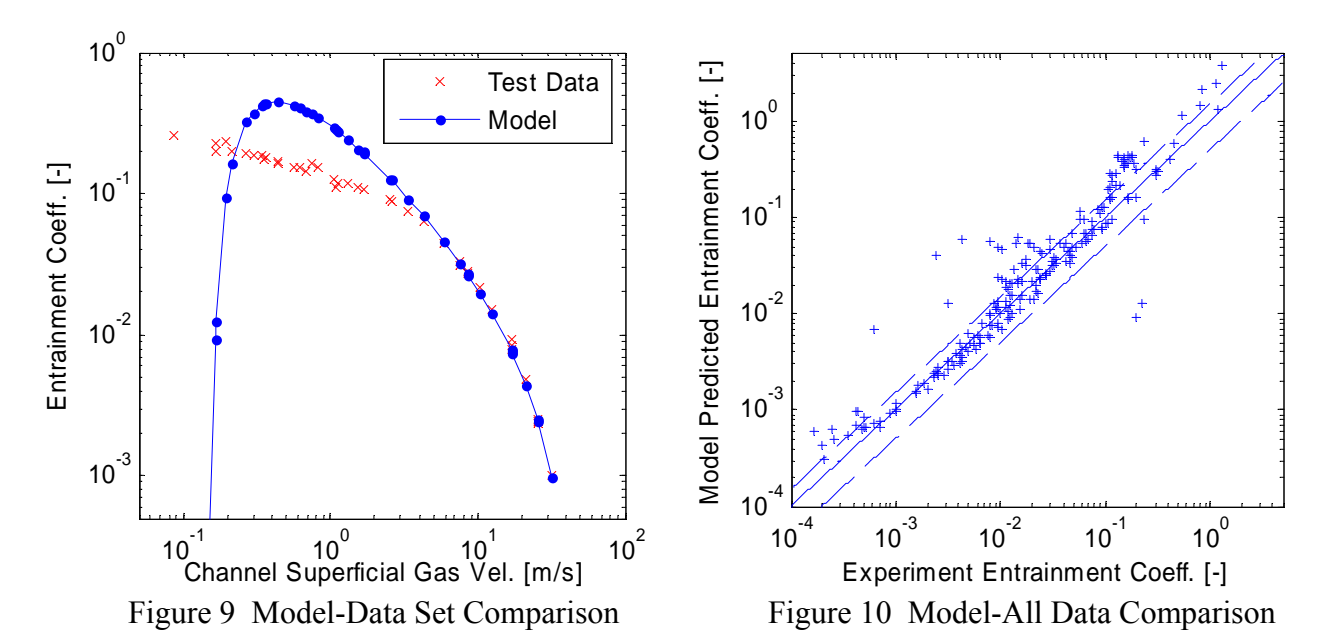
$$\Delta P_{\text{friction}} = \left(\frac{1}{(1-\alpha)^{n}}\right) \left(\frac{1}{2} \frac{f \cdot \delta_{\text{ch}}}{d_{\text{ch}}} \rho_{\text{m}} \cdot (j_{\text{m,ch}})^{2}\right) \text{ where } f = \begin{cases} 0.08 & \text{if } \text{Re}_{\text{m}} < 244.67 \\ 0.3164 \cdot \text{Re}_{\text{m}}^{-0.25} & \text{if } \text{Re}_{\text{m}} \ge 244.67 \end{cases}$$
(9)

$$\Delta P_{\text{sing}} = \frac{1}{2} \cdot K_{s} \cdot \rho_{m} \cdot j_{m,\text{ch}}^{2} + \frac{1}{2} \cdot K_{s} \cdot \rho_{g} \cdot j_{g,\text{ch}}^{2}$$
(10)

$$\Delta P_{acc} = \rho_{m} \cdot j_{m,ch} \cdot \left(\frac{j_{m,ch}}{1-\alpha}\right)$$
 (11)

$$j_{m,ch} = \sqrt{\frac{\delta_{ch} \cdot g \cdot [(S) - (1 - \alpha)]}{\left(\frac{1}{(1 - \alpha)^{n}} \cdot \frac{1}{2} \cdot \frac{f \cdot \delta_{ch}}{d_{ch}}\right) + \left(\frac{1}{1 - \alpha}\right) + \left(\frac{1}{2} \cdot K_{s} \cdot \left(1 + \frac{\rho_{g} \cdot j_{g,ch}^{2}}{\rho_{m} \cdot j_{m,ch}^{2}}\right)\right)}}$$
(12)

Figures 9 and 10 compare the entrainment coefficient predicted by the model to that obtained experimentally for one data set and 236 single channel data points from the UW entrainment facility. The data in Figure 10 covers the parameter range listed in Table 1. The model predicts 62.3% of the air-water data to within +/-50% and 49.7% of the data to within +/-25%. Zero entrainment, no liquid ejected, is predicted for 7 of the data points.



### 2. Flow Area

Several phenomena have been identified which may create or close eruption sites over the course of an MCCI. Previously, steady state limits of these phenomena were used as boundaries to define a region of possible flow area configurations (N<sub>ch</sub> and d<sub>ch</sub>), given a set of MCCI conditions [2]. Basic dynamic modeling which predicts the occurrence and timescales for two eruption site generation and three eruption site closing phenomena have been developed. Preliminary modeling of these phenomena was presented in [7]. The modeling for two of the dominate phenomena are included in this paper with the others being described in Sections 2.3 and 2.4. Currently, the channel diameter is user specified.

## 2.1 Crust failure due to local gas buildup

The concrete decomposition gasses may coalesce to form gas pockets beneath the crust which then migrate to eruption sites where they can be vented. The trapped and migrating gas pockets exert a force on the crust proportional to the bubble's buoyancy. This force can be sufficient to fail thin crusts.

Assuming the bottom of the crust is flat and horizontal, the thickness of a static gas bubble trapped below the crust can be found through relating the static pressure to the surface tension forces acting on the bubble, Eqn. (13). The pressure exerted by the trapped gas bubble onto the bottom of the crust is given by Eqn. (14). If the eruption sites are assumed to be evenly distributed, the maximum diameter of a trapped gas bubble between eruption sites is given by Eqn. (15). The maximum stress due to the uniform loading of a circular disk, of diameter d<sub>b.trapped</sub> is given by Eqn. (16) (Eqns. 66f and 71 of [8]). In the case of a floating crust, the edges of any sub-section of crust are not purely simply supported or clamped. This work assumed a conservative value of  $C_{\sigma}$  to be 1.238. If the maximum stress in the crust is equal to or greater than the failure stress of the crust ( $\sigma_{max} \geq \sigma_{cr,fail}$ ), the crust will fail creating eruption sites. Combining Eqns. (13-16) yields Eqn. (17) for the minimum number of channels which must be present such that a trapped gas pocket is not large enough to fail the crust locally. This modeling does not take into account the additional stresses in the crust due to thermal gradients. Crust failure by this mechanism is thought to occur rapidly. The timescale for local crust failure, Eqn. (18), is taken to be the time it takes to generate a bubble of thickness  $\delta_b$ , Eqn. (13). It is assumed if there is less than the minimum number of channels, the minimum number of channels will be created after the time given by Eqn. (18) has elapsed.

$$\delta_{b} = \frac{2 \cdot \gamma_{m}}{\rho_{m} \cdot g \cdot r_{b}} \left( \sqrt{1 + \frac{\rho_{m} \cdot g \cdot r_{b}^{2}}{\gamma_{m}}} - 1 \right) \text{ letting } r_{b} + \frac{\delta_{b}}{2} \approx r_{b}$$
 (13)

$$P_{b,trapped} \approx (\rho_m - \rho_g) \cdot g \cdot \delta_b \approx \rho_m \cdot g \cdot \delta_b$$
 (14)

$$d_{b,trapped} = \sqrt{\frac{4 \cdot A_{cr}}{\pi \cdot N_{ch}}}$$
 (15)

$$\sigma_{\text{max}} = \frac{C_{\sigma} \cdot P_{\text{b,trapped}}}{4} \left(\frac{d_{\text{b,trapped}}}{\delta_{\text{cr}}}\right)^2 \text{ where: } C_{\sigma} = \begin{cases} 0.75 & \text{simply supported edges} \\ 1.238 & \text{clamped edges} \end{cases}$$
 (16)

$$N_{\min, cr, fail} = \frac{4 \cdot A_{cr}}{\pi} \left( \frac{C_{\sigma} \cdot \gamma}{\delta_{cr}^2 \cdot \sigma_{cr, fail}} \right)^2 \left( \sqrt{1 + \frac{\rho_m \cdot g \cdot A_{cr}}{\pi \cdot \gamma \cdot N_{\min, cr, fail}}} - 1 \right)^2$$
(17)

$$t_{cr,fail} = \frac{\delta_b}{j_{g \text{ nool}} - j_{g \text{ cr}}}$$
 (18)

## 2.2 Melt freezing due to steady flooding of water

Flooding of water into the channels occurs if the gas velocity through the channel is below a minimum threshold. Wallis, [9], and Puskina and Sorokin, [10], provide expressions for the minimum gas velocity to prevent flooding, Eqns. (19, 20). Note the Puskina and Sorokin criterion is independent of the channel diameter in contrast to the Wallis criterion. When combined with a continuity equation for the gas flow, Eqn. (2), Eqn. (20) can be re-arranged to provide the maximum number of eruption sites in order to prevent flooding, Eqn. (21). A similar equation can be developed based on Wallis criterion. This assumes gas flow is steady and evenly distributed to the eruption site channels, neglects vaporization of the flooding water and capillary effects.

$$j_{g,flood,Wallis} = 0.5 \cdot \left( \frac{g \cdot d_{ch} \cdot (\rho_w - \rho_g)}{\rho_g} \right)^{1/2}$$
 (19)

$$j_{g,flood,PS} = 3.2 \cdot \frac{(g \cdot \gamma_w \cdot (\rho_w - \rho_g))^{1/4}}{(\rho_g)^{1/2}}$$
 (20)

$$N_{ch,PS} = 1.250 \cdot \left( \frac{\left( j_{g,pool} - j_{g,cr} \right) \cdot A_{cr}}{\pi \cdot d_{ch}^2} \right) \cdot \left( \frac{\rho_g}{g \cdot (\rho_w - \rho_g)} \right)^{1/4} \cdot \left( \frac{\rho_g}{\gamma_w} \right)^{1/4}$$
 (21)

If flooding of water into the channel were to occur, the channel walls and slugs of melt passing through the channel may quench. A rough time scale for channel plugging by water flooding is constructed based on the time it takes for a critical thickness of melt to freeze. A minimum thickness of melt is required to plug the channel and prevent gas from re-opening the channel. This minimum thickness is found using Eqn. (16) for the clamped edge condition based on the channel dimensions, Eqn. (22). The pressure exerted on the solidified web of crust is set equal to the driving pressure across the crust, Eqn. (23).

$$\delta_{\text{cr,web}} = \sqrt{1.238 \cdot \frac{P_{\text{under,crust}} \cdot d_{\text{ch}}^{2}}{4 \cdot \sigma_{\text{cr fail}}}}$$
 (22)

$$P_{under,crust} = g \cdot \left(\delta_{cr} \cdot \rho_{cr} + \delta_{pb} \cdot \rho_{pb}\right) \tag{23}$$

The time for a 1-D semi-infinite melt slug to freeze a thickness of  $\delta_{cr,web}$  is given by Eqn. (24), (from Eqn. 5.60 of [12]). This equation is solved iteratively for time 't' where 't' is the time for melt to freeze and 'erfc' is the complimentary error function. The convection coefficient for the top of the freezing melt slug, 'h', is estimated by the maximum of either the critical heat flux, Eqn. (25), (from Eqn. 10.7 of [11]), or thermal radiation heat transfer, Eqn. (26). If water is flooding into the channels (if  $j_{g,ch}$  is less than Eqn. (19) or (20)), then the number of channels which will freeze shut (after the time determined by Eqn. (26)) is assumed to be given by Eqn. (27). This equation essentially distributes the decomposition gases such that the maximum number of channels is at the flooding limit (stay open) with the remaining channels set to freeze shut.

$$\frac{T_{m,freeze}\left(\delta_{cr,web},t\right) - T_{m,initial}}{T_{m,freeze} - T_{m,initial}} = \operatorname{erfc}\left(\frac{\delta_{cr,web}}{2}\sqrt{\frac{\rho_{m} \cdot c_{p,m}}{k_{m} \cdot t}}\right) \dots \\
\dots - \left[\exp\left(\frac{h \cdot \delta_{cr,web}}{k_{m}} + \frac{h^{2} \cdot t}{k_{m} \cdot \rho_{m} \cdot c_{p,m}}\right)\right] \cdot \left[\operatorname{erfc}\left(\frac{\delta_{cr,web}}{2}\sqrt{\frac{\rho_{m} \cdot c_{p,m}}{k_{m} \cdot t}} + \frac{h}{k_{m}}\sqrt{\frac{k_{m} \cdot t}{\rho_{m} \cdot c_{p,m}}}\right)\right]$$
(24)

$$h_{chf} = \frac{0.149 \cdot i_{lv} \cdot \rho_{wv,sat}}{T_{m,ave} - T_{w,sat}} \cdot \left[ \gamma_w \cdot g \cdot \frac{\left(\rho_{lw,sat} - \rho_{wv,sat}\right)}{\left(\rho_{wv,sat}\right)^2} \right]^{1/4}$$
(25)

$$h_{rad} = \frac{\varepsilon_m \cdot \xi \cdot (T_{m,ave}^4 - T_{lw,sat}^4)}{T_{m,ave} - T_{lw,sat}}, \text{ where } T_{m,ave} = \frac{T_m + T_{m,freeze}}{2}$$
(26)

$$N_{\text{freeze,flood}} = N_{\text{ch}} - \frac{j_{\text{g,pool}} \cdot A_{\text{cr}}}{j_{\text{g,flood}} \cdot 0.25 \cdot \pi \cdot d_{\text{ch}}^2}$$
(27)

# 2.3 Additional modeled phenomena

Three additional eruption site creation or closure models have been developed and are described in [7]. A phenomenon was identified where cyclic buildup and collapse of foam beneath the crust can cause periodic loss of gas flow through the channel. If the gas flow intermittency is long enough, water could flood and freeze a melt slug within the channel. In addition to melt freezing in the channel due to flooding of water, the melt and gas mixture loses energy to the cooler channel wall as it passes through the eruption site, [5]. If the melt temperature decreases enough, the melt would freeze, plugging the channel. In addition to failure of the crust due to local gas pockets, sections of the crust may fail if large scale gas buildup occurs beneath the crusts. If there is insufficient flow area to vent the concrete decomposition gases through the crust, gas will build up. This trapped gas would either levitate a floating crust or pressurize beneath an anchored crust. The gas layer would also serve to insulate the underlying melt. Large scale gas build up is an unstable condition which would result in the creation of new eruption sites.

## 2.4 Additional non-modeled phenomena

Other phenomena have been identified that can impact the number of eruption sites [2]. For example, an upper limit on the number of channels could be developed in order to maintain crust structural integrity. In addition, a solid particle could plug an eruption site if it became lodged in the channel. Inclusion of these phenomena is limited by the uncertainty in system properties.

In addition to determining the number of eruption sites, the entrainment models in this work as well as [3, 4, 5] require either determining or specifying the channel diameter. A model developed by Farmer [5], used a heat transfer balance to find the steady-state channel diameter. Channel diameter evolution models have been investigated by the current authors; however, the models were very sensitive to thermal boundary conditions applied. For the current work, a specified fixed channel diameter is used. Further work in this area is needed.

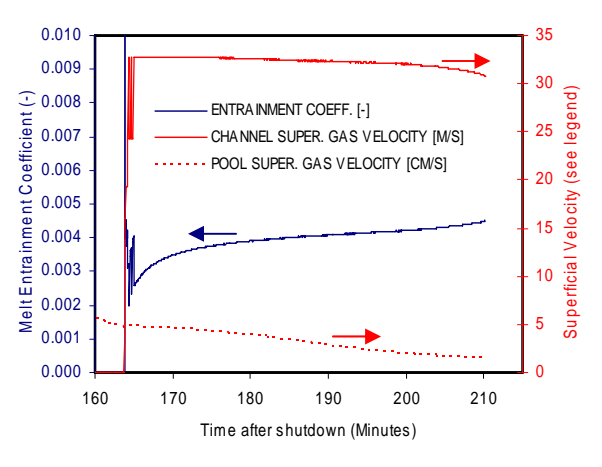
Finally, there is a question of determining what fraction of the ejected melt forms a particle bed versus forming solid cone-like mounds. The formation of a particle bed, in contrast to solid mounds, greatly impacts the long term coolability of the corium debris. During the M3b test, with a UO<sub>2</sub>-ZrO<sub>2</sub> melt, approximately 34% of the ejected melt formed an eruption mound with rest forming a particle bed [13]. In contrast, the ECOKATS-2 test, with an alumina melt, formed many eruption mounds and no particle bed [14]. The formation of eruption mounds and particle beds may be influenced by the thermal properties and fragmentation behavior of the melts. Future modeling work in this area is needed.

### 3. Synthesis

A dynamic melt eruption model, consisting of the melt entrainment model, Eqn. (12), and five dynamic eruption site creation or closure models (Section 2.2-2.4), were integrated into the CORQUENCH v3.03 MCCI systems code [12]. The new eruption model will be available in the next release version of CORQUENCH.

A sample MCCI calculation with the new eruption model is provided below. The core melt scenario is the base-case set of conditions described in [15] except for the Epstein\Lister water ingression and the UW melt eruption models were enabled. To summarize, a 75% PWR core melt is relocated onto limestone-common sand concrete 120 minutes after reactor shutdown. Top flooding of water starts 30 minutes after melt relocation. Currently, CORQUENCH does not account for crust porosity. When determining the crust submergence in the melt eruption model subroutine, a crust porosity of 10% was assumed. This value is consistent with post test analysis of the M3b crust and other tests [13]. The Puskina and Sorokin model was set as the default flooding model. All ejected melt was transformed into a uniform particle bed. The channel diameter was set to 1.0 cm. Figures 11 and 12 summarize the simulation results.

Qualitatively and possibly quantitatively, the melt eruption model produced results which are consistent with our understanding of MCCI and experimental observations. Initially, many eruption sites are formed due to the local crust loading (Section 2.1). This large number of eruption sites may represent the cracks between plates of crust observed during initial crust formation. As the crust thickens and the melt pool cools, the number of eruption sites decrease due to the water flooding criterion (Section 2.2). The predicted melt entrainment coefficient of  $(2-4.5\times10^{-3})$  is reasonable compared to those estimated for previous tests  $(0.04-2.5\times10^{-3})$  [2]). The predicted eruption site density (20-5 m<sup>-2</sup> after initial transient) is also reasonable in comparison to previous tests (2-10 m<sup>-2</sup> for MACE tests [5]) and (4-7.5 m<sup>-2</sup> for ECOKATS-2 [14]). Melt quenching occurs rapidly with the new melt eruption model, 46 minutes after crust formation; whereas, quenching occurs 630 minutes after crust formation if melt eruptions are prohibited. If the holes size is set to 0.5 cm instead of 1.0 cm, the predicted entrainment coefficient was about 2.5 times lower and the number of eruption sites was approximately 4 times higher (due to flooding criterion). If siliceous concrete (SIL) is used instead of LCS, the predicted entrainment coefficient is approximately 4 times less and the number of sites was about 2 times less. The reduced liquid ejection and number of eruption sites is consistent with observation of SIL type concrete tests [1, 2, 12].



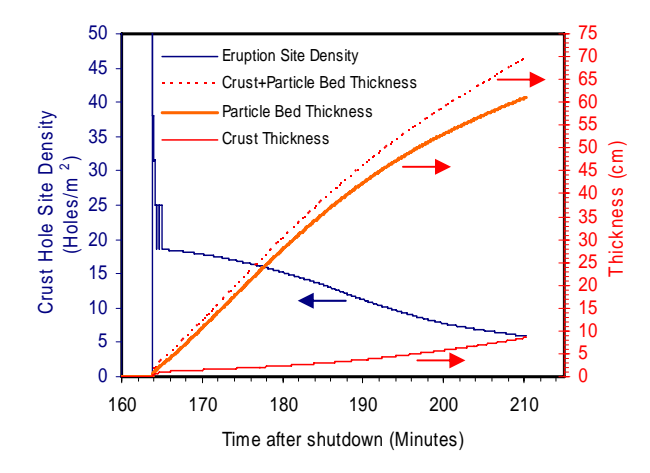


Figure 11 Entrainment Coefficient Prediction

Figure 12 Eruption Site Density Evolution

Due to the flooding criterion, the gas flow rate through each channel remains high, Figure 11. With such a high superficial gas velocity, the predicted gas void fraction in the channel ranges from 0.85-0.90. If the flooding criterion is used, a void fraction model capable of predicting high void fractions, such as the Dix model, Eqn. (8), is necessary.

During the period when melt eruptions were active, the viscosity of the melt ranged from 100 to 300 mPa s. Work is underway to verify the entrainment model against data in this range of viscosities. This may require changes to the entrainment model. Future work includes further refinement of the melt eruption entrainment and flow geometry models and comparison against the MCCI experimental database. Finally, the new melt eruption model will be integrated into the CORQUENCH MCCI systems code, [12], and will be available in the next release version.

## 4. Nomenclature

A	cross sectional area (m <sup>2</sup> )	3	emissivity (-)
$C_{\sigma}$	loading factor in Eqn (16) (-)	f	friction factor (-)
$c_p$	melt specific heat (m <sup>2</sup> s <sup>-2</sup> K <sup>-1</sup> )	γ	surface tension (kg s <sup>-2</sup> )
d	diameter (m)	δ	thickness (m)
g	gravity (m s <sup>-2</sup> )	ρ	density (kg m <sup>-3</sup> )
h	heat transfer coefficient (W m <sup>-2</sup> K)	σ	stress (kg m <sup>-1</sup> s <sup>-2</sup> )
$i_{lv}$	water liquid-vapor phase change enthalpy (m <sup>2</sup> s <sup>-2</sup> )	μ	viscosity (kg m <sup>-1</sup> s <sup>-1</sup> )
j	superficial velocity (m s <sup>-1</sup> )		
k	thermal conductivity (kg m s <sup>-3</sup> K <sup>-1</sup> )	Subscripts	
$K_s$	singular pressure drop coefficient ( - )	b	bubble
Ke	entrainment coefficient (-)	ch	channel
N	number of eruption sites (m <sup>-2</sup> )	cr	crust
P	pressure (kg m <sup>-1</sup> s <sup>-2</sup> )	freeze	freezing point
$Re_{m}$	melt Reynolds number (-) = $\frac{\rho_{\text{m}} \cdot J_{\text{ch}} \cdot d_{\text{ch}}}{}$	flood	flooding point
r	radius (m) $\mu_{\rm m}$	g	gas
S	submergence (-)	m	melt
t	time (s)	pb	particle bed
T	temperature (K)	pool	pool
Ÿ	volumetric flow rate (m <sup>3</sup> s <sup>-1</sup> )	sat	saturation point
α	gas void fraction ( - )	wv	water vapor
ξ	Stefan-Boltzmann constant (W m <sup>-2</sup> K <sup>-1</sup> )	lw	liquid water

### 5. References

- [1] Farmer, M.T., Kilskonk, D.J., Aeschlimann, R.W., "Corium Coolability Under Ex-Vessel Accident Conditions for LWRs," *Nuclear Engineering and Technology*, Vol. 41, No. 5, June 2009.
- [2] Robb, K. R., and Corradini, M. L., "Towards Understanding Melt Eruption Phenomenon during Molten Corium Concrete Interaction," Proc. of ICONE-18, ASME, May 17-21 Xi'an, China, 2010, paper 30116.
- [3] Tourniaire, B., Seiler, J. M., Bonnet, J. M., "Liquid Ejection Through Orifices by Sparging Gas the PERCOLA Program," Proc. of ICONE-10, ASME, USA, 2002, pp. 21.
- [4] Tourniaire, B., Seiler, J. M., Bonnet, J. M., "Experimental Study and Modelling of Liquid Ejection through Orifices by Sparging Gas," Nuclear Engineering and Design, 236(19-21), 2006 pp. 2281-95.
- [5] Farmer, M. T., "Phenomenological Modeling of the Melt Eruption Cooling Mechanism during Molten Corium Concrete Interaction (MCCI)," Proc. of ICAPP'06, ANS, June 4-8, Reno, NV, USA, 2006, pp. 1296-1305.
- [6] Coddington, P., Macian, R., "A Study of the Performance of Void Fraction Correlations used in the Context of Dift-Flux Two-Phase Flow Models," Nuclear Engineering and Design, 205, 2002, pg 199-216.
- [7] Robb, K. R., and Corradini, M. L., "Experimental and Theoretical Investigation of Melt Eruptions during MCCI," OECD/NEA MCCI Seminar 2010, November 15-17, Cadarache, France, paper S4.3.
- [8] Timoshenko, S., and Woinowsky-Krieger, S., "Theory of Plates and Shells," McGraw-Hill, New York, 1959.
- [9] Wallis, G.B., "One-dimensional two-phase flow," McGraw-Hill, New York, 1969.
- [10] Puskina, O.L., Sorokin, Y.L., "Breakdown of Liquid Film Motion in Vertical Tubes, Heat Transfer Sov. Res.," Vol.1, No. 5, 1969, pp 56-64.
- [11] Incropera, F. P., DeWitt, D.P., "Fundamentals of Heat and Mass Transfer," 5<sup>th</sup> ed., John Wiley & Sons, Hoboken, NJ, 2002.
- [12] Farmer, M.T., "The CORQUENCH Code for Modeling of Ex-Vessel Corium Coolability Under Top Flooding Conditions, Code Manual Version 3.03", OECD/MCCI-2010-TR03, Draft March 2010.
- [13] Farmer, M.T., Aeschlimann, R.W., Kilsdonk, D.J., "Results of the MACE Test M3b Posttest Debris Characterization," EPRI, ACEX-TR-C33, 2001.
- [14] Alsmeyer, H., Cron, T., Foit, J.J., Messer, G., Schmidt-Stiefel, S., Hafner, W., Kriscio, H., "Experiment ECOKATS-2 on melt spreading and subsequent top flooding: test and data report," FZKA 7084, SAM-ECOSTAR-D14/D16 D39/D40, Karlsruhe, Germany, 2005.
- [15] Robb, K. R., and Corradini, M. L., "MCCI Simulation Comparison Between MELCOR and CORQUENCH," NURETH-14, ANS, September 25-30, Toronto, Canada, 2011, paper 289.